

Mono- γ Production of a Vector Dark Matter at Future e^+e^- Collider

Kai Ma^{1,2,3,*}

¹*School of Fundamental Physics and Mathematical Science,
Hangzhou Institute for Advanced Study,
UCAS, Hangzhou 310024, Zhejiang, China*

²*University of Chinese Academy of Sciences (UCAS), Beijing 100049, China*

³*Department of Physics, Shaanxi University of
Technology, Hanzhong 723000, Shaanxi, China*

(Dated: May 12, 2022)

Abstract

Associated production of a dark particle and a photon, represented as a mono- γ event, is a promising channel to probe particle contents and dynamics in the dark sector. In this paper we study properties of the mono- γ production of a vector dark matter at future e^+e^- colliders. The photon-like and Pauli operators, as well as triple gauge bosons interactions involving the dark matter, are considered in the framework of Effective Field Theory. We show that, comparing to the Pauli operator, the triple gauge bosons couplings are much more interesting at high energy collider. Beam polarization effects are also analyzed, and we show that the experimental sensitivities can not be enhanced significantly because of the smaller luminosity.

* Electronic address: makai@ucas.ac.cn

CONTENTS

I. Introduction	3
II. Invisibility at e^+e^- Collider	5
III. Mono- γ Production	7
A. Differential and Total Cross Sections	8
B. Beam Polarization Effects	11
IV. Constraints from e^+e^- Experiments and a_e	12
A. BaBar	12
B. LEP-DELPHI	13
C. Anomalous Magnetic Dipole Moment	14
V. Significances at Future e^+e^- Colliders	15
A. Significances at CEPC	16
B. Significances at ILC	18
VI. Conclusion	20
Acknowledgments	21
References	21

I. INTRODUCTION

Gravitational effects of dark matter (DM) have been unambiguously observed in astrophysical and cosmological measurements [1–3]. Not only that, DM is also an excellent candidate of explaining some fundamental theoretical questions of the Standard Model (SM). There are also abnormalities, for instance the muon $g - 2$ [4], which can be accounted for by the DM. However it is certainly true that the particles that have been observed can not be the DM. Extending particle contents of the SM by adding new states which interact weakly with the SM particles is the most profound approach to study physical properties of the dark sector. It is highly desirable to adopt an approach of Effective Field Theory (EFT) involving the DM, the so called DM EFT (DMEFT) [5–7], to model-independently study physics of the dark sector. In general, the DM can take into play at both tree and loop level [8, 9], and a variety of theoretical models of DM have been proposed [10]. Lots of experimental searches for DM in direct [11], indirect [12] and collider signatures [13] have been conducted, but so far no clear evidence was reported.

In general, the DM can be scalar [14–18], fermion (Dirac or Majorana) [15–22] or vector state [15, 17, 18, 23]. In this work we focus on a vector model of the DM, whose kinematical Lagrangian is given as,

$$\mathcal{L}_X = -\frac{1}{4}X^{\mu\nu}X_{\mu\nu} + \frac{1}{2}m_X^2 X^\mu X_\mu, \quad (1)$$

where X_μ is the massive vector field with mass m_X , and $X_{\mu\nu}$ is its field strength. The Dark Photon (DP) model [24], in which a dark vector state interacts with the SM particles through a kinematical mixing term $\epsilon X^{\mu\nu}F_{\mu\nu}$ [24, 25], is a representation of this class. The photon component of the DM can induce decay into charged particles, and can be described by following effective operator,

$$\mathcal{O}_1 = e\epsilon \bar{\psi}\gamma^\mu\psi X_\mu. \quad (2)$$

In case of that the above kinematical mixing is the only building block of the DM model, the mixing parameter ϵ must be very small (with a typical value $\epsilon \sim 10^{-10}$) such that the theory is consistent with experimental measurements [26–30]. However, such strong constraint can be released if more new states are involved, for instance the Axion-like particles [31].

On the other hand, the DM can also couple to SM fermions at $D5$ via magnetic dipole

interaction (Pauli operator) [32–34],

$$\mathcal{O}_2 = \frac{1}{2\Lambda_2} \bar{\psi} \sigma^{\mu\nu} \psi X_{\mu\nu}, \quad (3)$$

where ψ is a charged fermion in the SM, and Λ_2 is the energy scale parameter. The above dipole interaction can appear at one-loop level in a UV completed model [32, 33]. Hence the energy scale Λ_2 is at the same order of mass of the heavy particles running in the loop, which should be a scale of new physics (NP), *i.e.*, $\Lambda_2 \sim M_{NP}$. In contrast to the photon-like operator Eq. (2), whose contribution to cross section of the mono- γ process decreases as $1/s$ at high energy, the Pauli operator Eq. (3) can initiate the mono- γ signal at a constant rate. Therefore, on dimensional analysis, significance of the Pauli operator is considerably larger than the one of the photon-like operator at high energy colliders, as long as the EFT description is valid. So far, lower bounds on the energy scale Λ_2 has not been reported. It was shown that future muon colliders with center of mass energy (CoM) $\sqrt{s} = 3 \text{ TeV}, 10 \text{ TeV}$ are expected to be good experiments to study it [34].

In this paper we study following triple gauge boson couplings,

$$\mathcal{O}_3 = \frac{1}{\Lambda_3^2} Z_{\mu\alpha} F^{\alpha\nu} X^\mu{}_\nu, \quad (4)$$

$$\mathcal{O}_4 = \frac{1}{\Lambda_4^2} Z_{\mu\alpha} F^{\alpha\nu} \tilde{X}^\mu{}_\nu, \quad (5)$$

$$\mathcal{O}_5 = \frac{1}{\Lambda_5^2} W_{\mu\alpha}^+ W^{-\alpha\nu} X^\mu{}_\nu, \quad (6)$$

$$\mathcal{O}_6 = \frac{1}{\Lambda_6^2} W_{\mu\alpha}^+ W^{-\alpha\nu} \tilde{X}^\mu{}_\nu, \quad (7)$$

where $F_{\mu\nu}$, $Z_{\mu\nu}$ and $W_{\mu\nu}^\pm$ are field strengths of the photon, neutral and charged weak bosons, respectively; $\tilde{X}_{\mu\nu}$ is the dual field strength of the DM, and $\Lambda_{3,4,5,6}$ are the energy scale parameters of the corresponding interactions. Here and after we will call these operators as DM triple gauge boson couplings (DMTGCs). Due to restriction of Bose statistics, the above operators can not exist in DMEFT where the DM field is included before breaking of the $SU_W(2) \times U_Y(1)$ gauge symmetry by the SM Higgs doublet [18]. Similar situation happens in neutral sector of triple gauge boson interactions within the SM contents [35–37], *i.e.*, couplings of $\gamma\gamma Z$, γZZ , ZZZ [38, 39]. Therefore, signals of such interactions indicate either that there are somehow enhancement effects in some higher dimensional operators containing those vertices, or that the NP scale is not so far away from the EW scale, such that the DM

field can be included effectively after the EW symmetry breaking [40]. The recently reported anomaly in the W boson mass measurement can be an indication of new physics near the EW scale [41]. On the other hand, when the DM couples to a SM current which is broken by the chiral anomaly, Wess-Zumino type interactions between X and the SM gauge bosons can appear when heavy fermions are introduced to cancel the anomaly [42]. Furthermore, in case of that X couples to purely right-handed currents [43], the triple interaction XWW will disappear, and only the coupling $XZ\gamma$ is allowed. Naively, experimental constraints on the charged sector of the DMTGCs are expected to be stronger, and can be further complicated if kinematical mixing between the DM and the photon is not neglected. In consideration of this, we will study this part elsewhere.

In this paper, we focus on the neutral sector of the DMTGCs. We will study the mono- γ production of X at future e^+e^- colliders, and our analysis includes photon-like and Pauli operators, as well as the DMTGCs. In general the vector X can be always invisible at the colliders by assuming that it couples dominantly to a completely dark sector, even through its interaction with the SM particles are non-zero. In Sec. II, we study invisibility of the vector X by assuming that the NP operators are the only available couplings bellow the scale under consideration, *i.e.*, Λ_i (or M_{NP}). This condition can give constraints on the scale parameters if the vector X is required to be invisible at the detector. In Sec. III, we study properties of the mono- γ events at e^+e^- colliders, including its differential cross sections (in Sec. III A), and beam polarization effects (in Sec. III B). In Sec. IV, we study constraints on the scale parameters by the BaBar experiment (in Sec. IV A), DELPHE experiment (in Sec. IV B) and anomalous magnetic dipole moments of the electron (in Sec. IV C). Experimental significances at future colliders, CECP and ILC, are studied in Sec. V. Conclusions are given in the final section, Sec. VI.

II. INVISIBILITY AT e^+e^- COLLIDER

In general, final state configuration for probing the DM at colliders depends on its invisibility, or its decay width Γ_X . If the DM decay with a relatively high rate, then it can be visible at the detector. The typical decay length of the X in mono- γ process at a CoM energy \sqrt{s} is given as,

$$L_X = \gamma_X \tau_X = \frac{\sqrt{s}}{2m_X \Gamma_X} \left(1 + \frac{m_X^2}{s}\right). \quad (8)$$

In case of that $m_X > 2m_\ell$ ($\ell = e, \mu, \tau$), the DM can decay into charged lepton pair via the photon-like and Pauli operators. The corresponding decay widths are given as,

$$\Gamma_1(X \rightarrow \ell^+ \ell^-) = \frac{m_X e^2 \epsilon^2}{12\pi} (1 + 2r_\ell^2) \sqrt{1 - 4r_\ell^2}, \quad (9)$$

$$\Gamma_2(X \rightarrow \ell^+ \ell^-) = \frac{m_X^3}{24\pi\Lambda_2^2} (1 + 8r_\ell^2) \sqrt{1 - 4r_\ell^2}, \quad (10)$$

where $r_\ell = m_\ell/m_X$. The rates of these two channels are roughly at the same order if $e\epsilon \sim m_X/\Lambda_2$. Since the DMTGC operators, anomalous decay, $Z \rightarrow X\gamma$, can happen when $m_X < m_Z$, and the corresponding decay width is given as,

$$\Gamma_{3(4)}(Z \rightarrow X\gamma) = \frac{m_Z^5}{144\pi\Lambda_{3(4)}^4} (1 + r_X^2) (1 - r_X^2)^3, \quad (11)$$

where $r_X = m_X/m_Z$. Neglecting the 3-body decay channel, $X \rightarrow Z^*\gamma \rightarrow f\bar{f}\gamma$, then X decay invisibly. The L3 [44] and DELPHI [45] collaborations at the LEP experiment have searched for single photons at the Z resonance. and obtain an upper limit on the branching ratio, $\mathcal{B}_{Z \rightarrow X\gamma} < 10^{-6}$. This bound can exclude a parameter space in the $\Lambda_{3(4)} - m_X$ plane. We will discuss this in details in Sec. V.

On the other hand, the DMTGC operators can initiate 3-body decays at elementary particle level, $X \rightarrow Z^*\gamma \rightarrow f\bar{f}\gamma$, with fermion f being leptons, neutrinos or quarks. Such processes are suppressed by m_X^4/m_Z^4 , hence it is much smaller unless m_X is very closer to m_Z . In case of $f = q$, the 2-body hadronic decay channels $X \rightarrow h\gamma$ can give non-trivial contribution. We will study these hadronic decay channels in a separate work. For this moment, let us focus on the on-shell two-body decay $X \rightarrow Z\gamma$, which pops up if $m_X > m_Z$. The corresponding decay width is given as,

$$\Gamma_{3(4)}(X \rightarrow Z\gamma) = \frac{m_X^5}{144\pi\Lambda_{3(4)}^4} (1 + r_Z^2) (1 - r_Z^2)^3, \quad (12)$$

where $r_Z = m_Z/m_X$. The width is suppressed by a factor of $m_X^4/\Lambda_{3,4}^4$.

When we study experimental significance in Sec. V, we will implement all the above results by requiring its decay length is smaller than a typical value, say $L_X < 1\text{m}$ or so, depending on real configuration of the detector.

III. MONO- γ PRODUCTION

In this section we study the mono- γ signals at e^+e^- colliders, *i.e.*, the process $e^+e^- \rightarrow \gamma X$. The representative Feynman diagrams are shown in Fig. 1(a)-1(c). In cases of the photon-like and Pauli operators, the photon is generated via initial state radiation, while for the DMTGC operators photon can be produced via a s -channel exchange of a (virtual) Z -boson. The invisible X results in a missing transverse energy at the detector. The dominant irreducible SM background is production of single photon in association with a neutrino pair, *i.e.*, $e^+e^- \rightarrow \gamma\nu\bar{\nu}$. However, different from pair production of fermionic DM (or production of a single fermionic DM in company with a neutrino), where invariant mass of the missing momentum has a continuous distribution, it is peaked at m_X in our case because there is only one invisible particle. This can reduce significantly the background, and the efficiency depends on precisions of momentum measurement of the γ , beam energy spectrum, *etc.* . We will consider such effects in Sec. V, where experimental significances of the signals are studied. On the other hand, one of the advantages of the e^+e^- collider is that the beam particles can be polarized. So, before analyzing experimental sensitivities, let us discuss production properties of the signals, including differential cross section given in Sec. III A, and beam polarization effects given in Sec. III B.

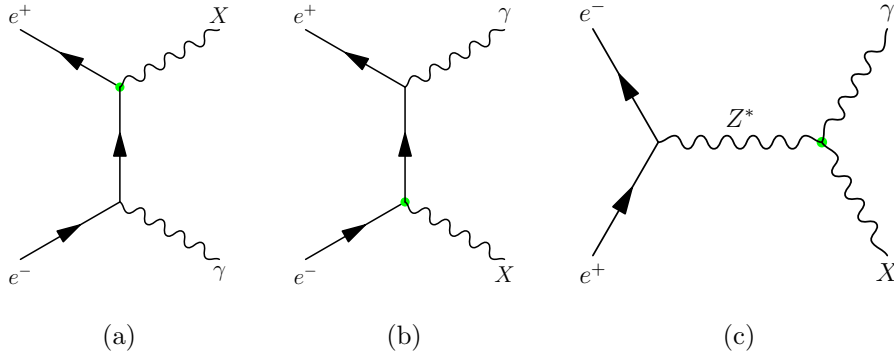


FIG. 1. Feynman diagrams of the mono- γ production at e^+e^- collider. Fig. 1(a) and Fig. 1(b) stand for initial state radiations of a photon, and can be induced by the operators Eq. (2) and Eq. (3). In contrast, the DMTGC operators, Eq. (6) and Eq. (7), can generate a photon via exchange of a (virtual) Z -boson in s -channel, as shown in Fig. 1(c).

A. Differential and Total Cross Sections

In this section we study total and differential cross section of the signals. In massless limit of the beam particles, the polarized differential cross sections are given as,

$$\frac{d\sigma_{1,\pm\mp}}{d\cos\theta_\gamma} = \frac{e^2\epsilon^2}{4\pi s(1-z_X^2)\sin^2\theta_\gamma} \left[(1+z_X^4)(1+\cos^2\theta_\gamma) + 2z_X^2\sin^2\theta_\gamma \right], \quad (13)$$

$$\frac{d\sigma_{2,\pm\pm}}{d\cos\theta_\gamma} = \frac{1}{\pi\Lambda_2^2(1-z_X^2)} \left[(1-z_X^2)^2 + 2z_X^4 + z_X^2(1+z_X^4)\cot^2\theta_\gamma \right], \quad (14)$$

$$\frac{d\sigma_{3(4),\pm\mp}}{d\cos\theta_\gamma} = \frac{e^2(g_V \mp g_A)^2 s (1-z_X^2)^3}{64\pi\Lambda_{3(4)}^4 [(1-z_Z^2)^2 + z_Z^4 y_Z^2]} \left[\sin^2\theta_\gamma + \frac{1}{2}z_Z^2(1+\cos^2\theta_\gamma) \right], \quad (15)$$

where $z_X = m_X/\sqrt{s}$, $z_Z = m_Z/\sqrt{s}$ and $y_Z = \Gamma_Z/m_Z$; θ_γ is polar angle of the photon in the Lab. frame where the z -axis is defined along to flying direction of the incoming electron; $\sigma_{i,\lambda_{e-}\lambda_{e+}}$ are cross section with helicities $\lambda_{e-}, \lambda_{e+} = \pm 1$ for electron and positron, respectively. Thanks to spin conservation, the photon-like and DTGC operators can give non-zero contributions only when $\lambda_{e-} = -\lambda_{e+}$, while for the Pauli operator only helicity combinations with $\lambda_{e-} = \lambda_{e+}$ survive. In addition, since parity violation of the electroweak neutral current in the SM, σ_{+-} and σ_{-+} has a difference depending on product between vector and axial-vector couplings, *i.e.*, $g_V g_A$ of the electron (see Eq. (15)).

We can also see that there are singularities at $\theta_\gamma = 0, \pi$ for the photon-like operator, similar to the well-known property of the background. Such singularity disappears in channels induced by the Pauli and DMTGC operators. In order to avoid those kinematical space, we implement our operators into **FeynRules** [46], and using **MadGraph5** [47] to estimate cross sections with following kinematical cuts,

$$|\eta_\gamma| \leq 3.35, \quad p_{T,\gamma} > 1 \text{ GeV}. \quad (16)$$

Fig. 2(a) shows polar angle distributions of the signal and background with above kinematical cuts at a typical center of mass energy $\sqrt{s} = 500 \text{ GeV}$, and for the signal we have set $m_X = 0$, $e\epsilon = 0.1$, and $\Lambda_i = 1 \text{ TeV}$ for reference. Signal of the photon-like operator is much similar to the background. However, the Pauli operator possesses a constant polar angle distribution, as can be seen from Eq. (14) in case of $z_X = 0$. For the DMTGC operators, the two operators have completely the same distribution, as we can see from Eq. (15). However, signal events are dominated in the central region of the detector. This is completely different

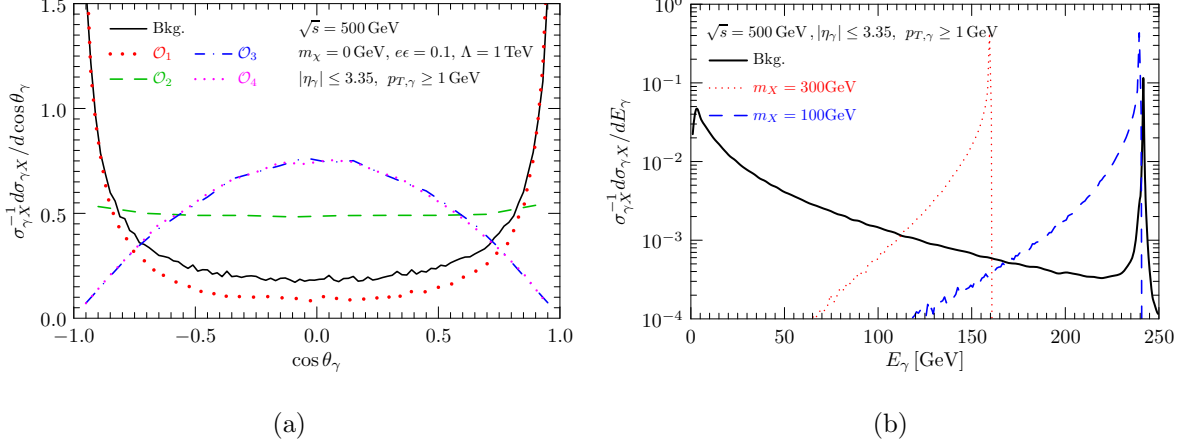


FIG. 2. *Fig. 2(a): normalized distributions of the polar angle of the photon in the CoM frame with $\sqrt{s} = 500$ GeV and $m_X = 0$ GeV. Fig. 2(b): normalized distributions of the energy of the photon in the CoM frame with $\sqrt{s} = 500$ GeV. Since E_γ is determined by purely kinematical condition, distributions of E_γ for the signals are illustrated by the DMTGC operators with $m_X = 100$ GeV and $m_X = 300$ GeV. In addition we have put kinematical cuts $|\eta_\gamma| < 3.35$ and $p_{T,\gamma} > 1$ GeV in both plots.*

from the background, and results in a higher kinematical selection efficiency. Furthermore, this property is purely because of transverse part contribution of a spin-1 particle exchanged in s -channel, and hence is independent on mass of the DM, m_X (see Eq. (15)). The above polar angle distributions can be used to distinguish the new physics operators, and we will discuss the details in Sec. V.

Neglecting practical limitations on experimental measurements, energy of the radiated photon has a fixed value for the signal. For CoM energy \sqrt{s} it is given as,

$$E_\gamma = \frac{1}{2}\sqrt{s} \left(1 - \frac{m_X^2}{s} \right). \quad (17)$$

This is determined by purely kinematical conditions, the photon has the same energy E_γ for all operators. However, photons of the background have a continuous energy spectrum dominated at soft region, as shown in Fig 2(b). The peak at $(1 - m_Z^2/s)\sqrt{s}/2 \approx 241.7$ GeV is due to the resonant channel $e^+e^- \rightarrow Z(\nu\bar{\nu})\gamma$. This can introduce a problem for probing signals when m_X is near m_Z . The situation gets worse if $\sqrt{s} \gg m_Z, m_X$, in which case $E_\gamma \sim \sqrt{s}/2$ for both signals and background. In any case, since energy of the signal is always peaked at E_γ , background events can be suppressed by a factor of 10^{-1} to 10^{-4} , depending on mass of the DM. Nevertheless, Due to Initial State Radiation (ISR) and

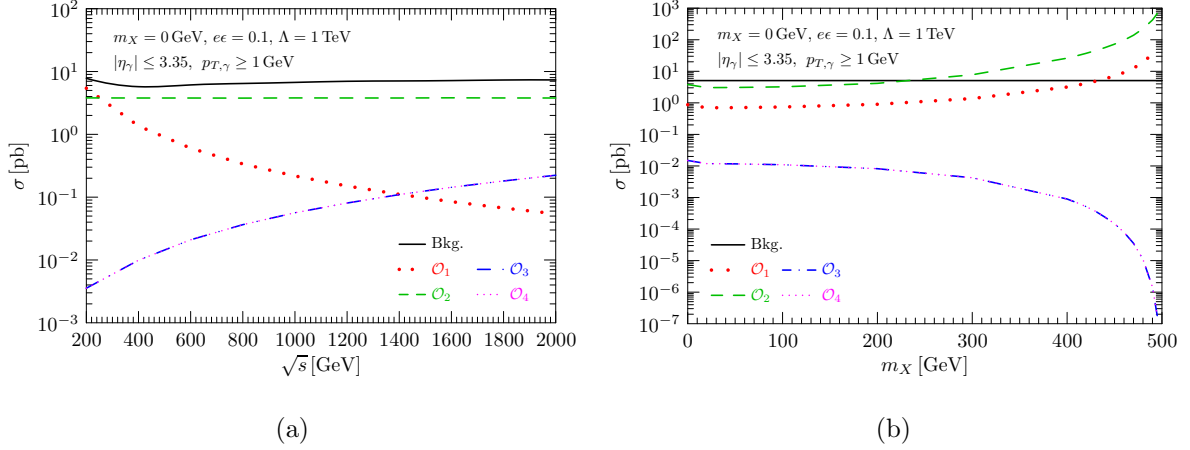


FIG. 3. *Fig. 3(a)*, cross sections of mono-photon productions with respect to center of mass energy \sqrt{s} for $m_X = 0$ GeV, $e\epsilon = 0.1$ and $\Lambda_i = 1$ TeV. *Fig. 3(b)*, mass dependences of the total cross section at $\sqrt{s} = 500$ GeV for $e\epsilon = 0.1$ and $\Lambda_i = 1$ TeV. In addition we have put kinematical cuts $|\eta_\gamma| < 3.35$ and $p_{T,\gamma} > 1$ GeV in both plots.

emission of beamstrahlung photons [48], beam energies are characterized by continuous spectra. Energy of the photon is hence smeared. In Fig 2(b), distributions of E_γ for \mathcal{O}_3 are shown for $m_X = 100$ GeV and 300 GeV. The ISR effect is taken into account by using the plugin MGISR [49, 50] to the MadGraph. We can see clearly the smearing effect. It turns out that selection efficiency of the signal is reduced.

Fig. 3(a) and 3(b) show CoM energy and mass dependences of the total cross section, respectively. we can see that, while cross section of the photon-like operator is dominant at low energy, and the one of the Pauli operator keeps a constant in the whole range of \sqrt{s} , contributions of the DMTGC operators grow quickly with increasing CoM energy. On the other hand, cross section of the background is reduced slightly from $\sqrt{s} = 200$ GeV to $\sqrt{s} = 400$ GeV. This behavior closely related to the resonance channel $e^+e^- \rightarrow Z(\nu\bar{\nu})\gamma$. The cross section reaches roughly a constant at high energy region. For the DMTGC operators, the m_X dependence shows a normal kinematical suppression at large mass region. However, for both the photon-like and Pauli operators the distributions show an enhancement as $m_X \rightarrow \sqrt{s}$. This is due to soft singularity (in massless limit of the incoming electrons), as can be seen in Eq. (13) and Eq. (14) (there is a factor $1 - z_X^2$ in the denominator in both cases).

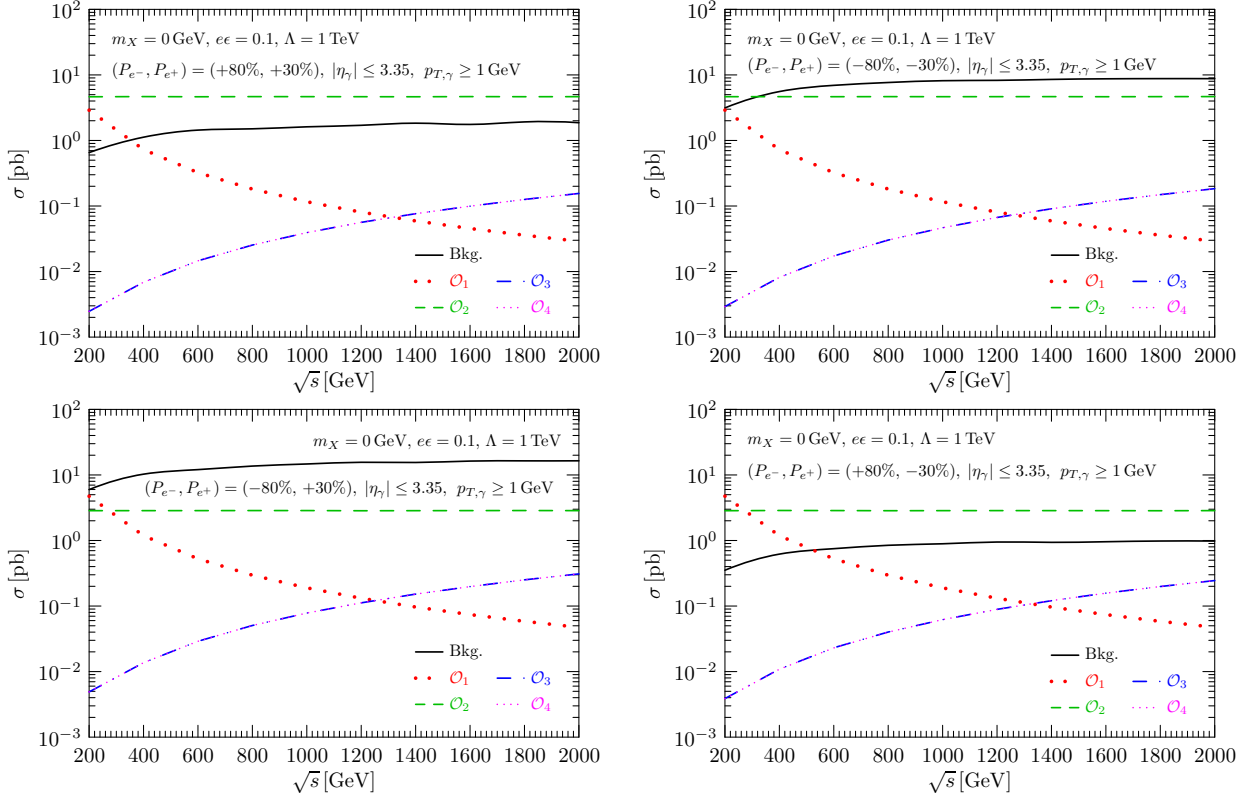


FIG. 4. Energy dependences of the cross sections with beam polarizations $(P_{e^-}, P_{e^+}) = (+80\%, -30\%)$ (top-left panel), $(-80\%, -30\%)$ (top-right panel), $(-80\%, +30\%)$ (bottom-left panel), and $(+80\%, -30\%)$ (bottom-right panel), respectively. Signals are shown with $m_X = 0$ GeV, $e\epsilon = 0.1$ and $\Lambda_i = 1$ TeV.

B. Beam Polarization Effects

One of the most advantages of the e^+e^- collider is that the beam particles can be polarized. Since the background contributes mainly through chiral couplings of the SM, particularly the $e\nu W$ coupling at high energy region, polarized beams are much help to reduce the background. The cross section with electron beam polarization P_{e^-} and positron beam polarization P_{e^+} are given by,

$$\sigma(P_{e^-}, P_{e^+}) = \frac{1}{4} \sum_{\lambda_{e^-}, \lambda_{e^+} = \pm 1} (1 + \lambda_{e^-} P_{e^-}) (1 + \lambda_{e^+} P_{e^+}) \sigma_{\lambda_{e^-} \lambda_{e^+}}, \quad (18)$$

where $\sigma_{\lambda_{e^-} \lambda_{e^+}}$ are cross sections with 100% polarizations, and for signals they are given in Eq. (13) -Eq. (15). Fig. 4 shows the polarized cross sections with typical polarization $P_{e^-} = \pm 80\%$ and $P_{e^+} = \pm 30\%$. For the background, the cross sections are shown without

contributions of the resonance channel ($e^+e^- \rightarrow Z(\nu\bar{\nu})\gamma$), which is less affected by beam polarizations, and is inessential when E_γ is not closer to E_γ^Z . The rest contributions come from the left-handed charged currents in the SM, the dominant background is σ_{-+} . Hence $\sigma_{\text{Bkg}}(-80\%, +30\%)$ is the largest one, as shown in the bottom-left panel. The other polarized channels are roughly suppressed by a factor from 0.06 to 0.54. For the Pauli operator, chirality is flipped in the neutral current, $\sigma_{\pm\pm}$ are the only non-zero contributions. Hence the largest polarized channels are $\sigma_2(\pm 80\%, \pm 30\%)$, the others are suppressed by a factor of about 0.61. In contrast, for both photon-like and DMTGC operators, the non-vanishing 100% polarized cross sections are $\sigma_{\pm\mp}$. This property results in the largest contributions $\sigma_{1,3,4}(\pm 80\%, \mp 30\%)$. Contributions of the other polarization configurations are reduced by a factor of about 0.61.

IV. CONSTRAINTS FROM e^+e^- EXPERIMENTS AND a_e

In this section we study constraints on the various NP operators by searches at the Bar-
Bar [51] and DELPHI [52] experiments, as well as measurements of the anomalous magnetic dipole moment of the electron [53, 54]. There are also astrophysical and cosmological constraints [42], particularly bounds on the photon-like operator are very strong [31], but we don't consider those limits here.

A. BaBar

The BaBar experiment with CoM energy of 10.58 GeV at the PEP-II B-factory has searched for dark photon by mono- γ events with a total luminosity of 53 fb^{-1} [51]. A search for dark photon in the resonance channel [55], $e^+e^- \rightarrow \gamma X$, $X \rightarrow \ell^+\ell^-$ ($\ell = e, \mu$) was also conducted by the BaBar Collaboration. However, exclusion limits in this channel depend on branching ratio of the decay $X \rightarrow \ell^+\ell^-$. Here we re-interpret mono- γ results for the Pauli and DMTGC operators. The single photon was required to have a polar angle in the following range,

$$-0.4 < \cos \theta_\gamma < 0.6 \text{ for } m_X < 5.5 \text{ GeV}, \quad (19)$$

$$-0.6 < \cos \theta_\gamma < 0.6 \text{ for } m_X > 5.5 \text{ GeV}, \quad (20)$$

in the CoM frame. Here $m_X = 5.5 \text{ GeV}$ is the critical value for defining low ($m_X < 5.5 \text{ GeV}$) and high mass ($m_X > 5.5 \text{ GeV}$) regions. In addition, photon is further selected by the cuts $E_\gamma > 3 \text{ GeV}$ and $E_\gamma > 1.5 \text{ GeV}$ in the low and high mass regions, respectively. The cuts $E_\gamma > 3(1.5) \text{ GeV}$ are helpful to reduce background, but are useless for signals since the polar angle requirements have rejected the events with $E_\gamma \lesssim 3.86 \text{ GeV}$ in the low mass region and $E_\gamma \lesssim 2.27 \text{ GeV}$ in the high mass region (with $m_X < 8 \text{ GeV}$ which corresponds to the maximum searched by the experiment). Hence we will ignore effects of the cuts on E_γ . On the other hand, as we have seen in Fig. 2(a) that polar angle distributions of the operators are completely different, therefore, efficiencies of the geometric cuts can be very different. The BaBar Collaboration used Boosted-Decision-Tree (BDT) based on characteristics of E_γ and $\cos \theta_\gamma$ to select signals. Here we consider only the effects of the geometric cuts, and are accounted for by implementing the cuts at generator level. The corresponding acceptance efficiencies are estimated at selected representative points ($\epsilon = \epsilon_{\text{BarBar}}, m_X = m_X^{\text{BarBar}}$) on the 90%C.L. exclusion line of the BaBar. Assuming that the trigger and reconstruction efficiencies of the photon are the same for all the operators, then for given mass $m_X = m_X^{\text{BarBar}}$, the 90%C.L. lower limits on the energy scales Λ_i are given as,

$$\Lambda_i \geq \left[\frac{\sigma_i(\Lambda_i = 1 \text{ GeV}, m_X = m_X^{\text{BarBar}})}{\sigma_1(\epsilon = \epsilon_{\text{BarBar}}, m_X = m_X^{\text{BarBar}})} \right]^{1/\kappa} [\text{GeV}], \quad (21)$$

where $\kappa = 2, 4$ for $i = 2, 3(4)$, respectively; and the cross sections are calculated after the geometric cuts. Our results will be shown in Sec. V.

B. LEP-DELPHI

Constraints on emission of an invisible graviton from low-scale extra-dimension and supersymmetric models were studied by the DELPHI experiment at LEP [52], and has been re-interpreted as limits on Dark Matter, for instance, in Ref. [56]. The DELPHI data was obtained with different CoM energies [57], ranging from 180.8 GeV to 209.2 GeV. The single-photon events were selected by three different triggers: the High density Projection Chamber (HPC), the Forward ElectroMagnetic Calorimeter (FEMC) and the Small angle Tile Calorimeter (STIC). Here we focus on the HPC which covers a wider range of E_γ ,

$$45^\circ < \theta_\gamma < 135^\circ, \quad 0.06 E_{\text{Beam}} < E_\gamma < 1.1 E_{\text{Beam}}, \quad (22)$$

comparing to FEMC and STIC. However, the HPC module has relatively lower trigger efficiency and worse energy resolution. The trigger efficiency strongly depends on the photon energy, and is about 52% at $E_\gamma = 6$ GeV and above 77% when $E_\gamma > 30$ GeV, and reached a maximum 84% when $E_\gamma \simeq E_{\text{Beam}}$. Since energies of the photons generated with parameters considered in this paper are almostly larger than 20 GeV, we will use a constant trigger efficiency $\epsilon^{\text{Trig}} = 80\%$ in our analysis. Furthermore, energy of the mono- γ (given by Eq. (17)) can also be significantly smeared by the energy resolution, particularly for hard photons (or equivalently smaller m_X). It turns out that selection efficiencies of the signals decrease in the low m_X region. In our following analysis, we require $|E_\gamma - E_\gamma(m_X)| < 1$ GeV, and energy dependence of the efficiency due to energy resolution was taken into account by the systematical uncertainty $\pm 8\%$ [57]. The experimental significances are estimated by calculating following χ^2 function,

$$\chi^2 = \sum_{i,j} \left[\frac{N_{\text{Sig}}(\sqrt{s_i}, \bar{\theta}_j)}{\sqrt{N_{\text{Bkg+Sig}}(\sqrt{s_i}, \bar{\theta}_j) + \Delta\sigma_{\text{Syst}}^2 \cdot N_{\text{Bkg}}^2(\sqrt{s_i}, \bar{\theta}_j)}} \right]^2, \quad (23)$$

where $N_{\text{Bkg/Sig/Bkg+Sig}}(\sqrt{s_i}, \bar{\theta}_j) = \mathcal{L}_i \cdot \epsilon^{\text{Trig}} \cdot \sigma_{\text{Bkg/Sig/Bkg+Sig}}(\sqrt{s_i}, \bar{\theta}_j)$ are number of events of the background, signal and summation of the background and signal, respectively; and polar angle distribution has also been binned in order to enhance the significance, and $\bar{\theta}_j$ stands for $c_{j-1} < |\cos \theta_{\gamma,j}| < c_j$ with c_j being the boundary values of the bin. The results will be discussed in Sec. V.

C. Anomalous Magnetic Dipole Moment

Discrepancy between theoretical prediction and experimental measurements in the magnetic dipole moment of the muon has been reported long ago (we refer to Refs. [58, 59] for recent reviews). Combination of the recent measurements by the FNAL Muon $g - 2$ experiment [60] and the old BNL result [61] has pushed the discrepancy to a level of 4.2σ . Implications of this anomaly have been widely studied. In this paper we focus on the anomalous magnetic dipole moment of the electron. Improved measurement of the fine structure constant by a matter-wave interferometer of cesium-133 atoms [62] shows a 2.4σ tension with the SM prediction [63],

$$\Delta a_e \equiv a_e^{\text{Exp}} - a_e^{\text{SM}} = -(8.8 \pm 3.6) \times 10^{-13} \quad (\text{Berkeley-2018}). \quad (24)$$

The important thing is that it has a different sign from the Δa_μ . Even though it is still suggestive, such a discrepancy challenges theoretical models which try to explain both Δa_e and Δa_μ simultaneously. However, the most recent atomic physics measurement of α_{em} using Rubidium-87 atoms implies [53, 54],

$$\Delta a_e \equiv a_e^{\text{Exp}} - a_e^{\text{SM}} = +(4.8 \pm 3.0) \times 10^{-13} \quad (\text{LKB-2020}), \quad (25)$$

which is more than 4σ away from the Berkeley-2018 result. More interestingly, the deviation is positive, has the same sign with the Δa_μ . Even though experimental uncertainties are at the same level, it is clear that further improved measurements are necessary to clarify the discrepancies reported in these two experiments, and consistent experimental results can be expected in forthcoming years. In following analysis we ignore this sign problem, and use the result given in Eq. (25) to study constraints on the mixing parameter ϵ . Contribution of the photon-like operator to Δa_e is given as [23, 64],

$$\Delta a_e^X = \frac{e^2 \epsilon^2}{4\pi^2} r_e^2 F_X(r_e), \quad (26)$$

where $r_e = m_e/m_X$, and the function $F_X(r_e)$ is given as,

$$F_X(r_e) = \frac{1}{2} \int_0^1 dx \frac{2x^2(1-x)}{(1-x)(1-r_e^2 x) + r_e^2 x}, \quad (27)$$

which is always positive.

V. SIGNIFICANCES AT FUTURE e^+e^- COLLIDERS

In practical measurement, energy of the photon can be smeared by, for instance, ISR of the beams and beamstrahlung emission of the photons [67]. In order to avoid overestimation of the experimental sensitivities, and also to select most of the signal events, the above detector activity should be taken into account. Take ILC as an example [67], it was shown that nearly 70% of the beam particles have energy lying in the window $|E_{\text{Beam}} - 250 \text{ GeV}| \leq 1 \text{ GeV}$, see also our simulation results in Fig. 2(b). In following calculations of experimental sensitivity, we estimate both signal and background events by assuming that the beam energy has a fixed value $\sqrt{s}/2$, and cross section of the signal is multiplied by an efficiency factor, $\epsilon_{\text{ISR}} = 70\%$, no matter which collider is under considering. Furthermore, the background is estimated by collecting all the cross sections as long as energy of the photon lies in the

window $|E_\gamma^{\text{Bkg}} - E_\gamma^{\text{Sig}}| < 1 \text{ GeV}$. The above simple approximation does not capture all signal (and also background) information, but much conservative it is. On the other hand, as we have shown that in Fig. 2(a), polar angle of the photon is much sensitive to the signal, and hence useful to enhance the experimental sensitivities. In consideration of this, distribution of the variable $\cos\theta_\gamma$ is divided into 10 bins, and the experimental significance is estimated by calculating following χ^2 function,

$$\chi^2 = \sum_i \frac{\left(\epsilon_{\text{ISR}} \cdot N_i^{\text{Sig}}\right)^2}{N_i^{\text{Bkg}} + \epsilon_{\text{ISR}} \cdot N_i^{\text{Sig}} + \left(\epsilon_{\text{Syst}} \cdot N_i^{\text{Bkg}}\right)^2}, \quad (28)$$

where N_i^{Sig} and N_i^{Bkg} are signal and background events in the i -th bin, ϵ_{Syst} stands for systematic uncertainty which can reduce the sensitivity significantly as shown in Ref. [68]. We also assume that $\epsilon_{\text{Syst}} = 1\%$ in following calculations. The radiative BhaBha process can also contribute the background. However such contribution can be significantly reduced by requiring that there is only one reconstructed BeamCal cluster, as reported in Ref. [67]. So, we will neglect the background coming from radiative BhaBha process.

A. Significances at CEPC

The CEPC experiment is designed to be a Higgs factory [69], but is also relevant for probing particles and dynamics in dark sector [70]. Three different running modes at the CEPC have been proposed [69]. In this study we focus on the mode with $\sqrt{s} = 240 \text{ GeV}$, in which a total luminosity of 5.6 ab^{-1} will be accumulated at two interaction points for 7 years of running. There are also other e^+e^- colliders, for instances, ILC, FCC-ee and CLIC running at a similar CoM energy. Here we chose the CEPC as a representative one for probing the operators considered in this paper. In our simulations, following kinematical cuts are used to estimate the signal significance defined in Eq. (28) ,

$$p_{T,\gamma} > 0.5 \text{ GeV}, \quad |\eta_\gamma| < 2.65. \quad (29)$$

Fig. 5(a), Fig. 5(b) and Fig. 5(c) show our results for the operators \mathcal{O}_1 , \mathcal{O}_2 and $\mathcal{O}_{3(4)}$, respectively.

The shaded region in blue represents $L_X > 0.1m$ with assumption $Br(X \rightarrow \ell^+\ell^-) = 1$. As we have mentioned, this condition can be released if the particle X decays into dark

particles. For reference, we also show the contour with $L_X = 1m$ in dashed-blue line. The gray region in the Fig. 5(a) is obtained by data extracted from Ref. [51], and stands for a 90%CL excluded region by the BaBar experiment. The gray region in Fig. 5(b) is obtained by reinterpreting the same data for the operator \mathcal{O}_2 , based on the method explained in Sec. IV A. For the operator $\mathcal{O}_{3(4)}$, due to suppression of the s/m_Z^2 , constraint from the

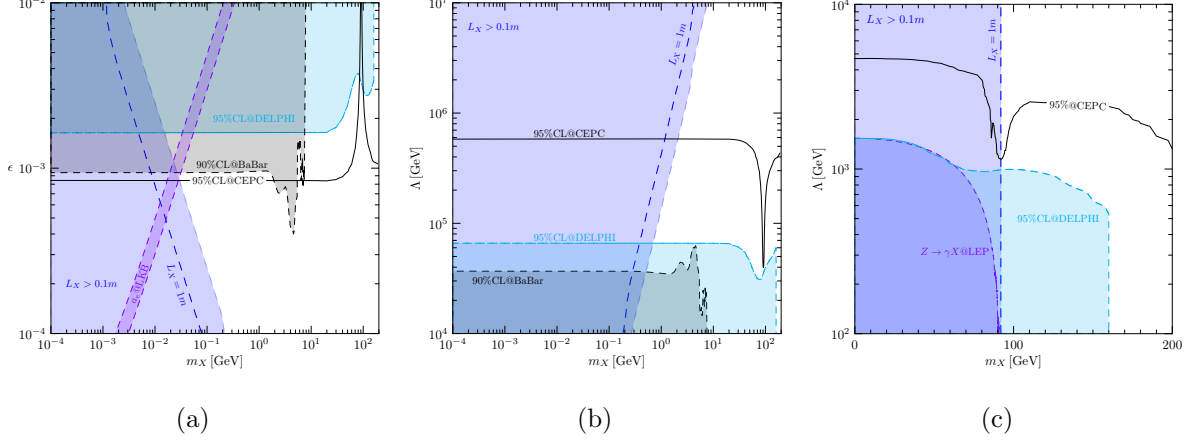


FIG. 5. Expected sensitivities at 95%CL for the operators \mathcal{O}_1 (Fig. 5(a)), \mathcal{O}_2 (Fig. 5(b)) and $\mathcal{O}_{3(4)}$ (Fig. 5(c)) at the CEPC with a total luminosity 5.6 ab^{-1} . The shades regions represents constraints from other experiments, and explained in the text.

BaBar experiment is rather weak, and the excluded region is outside of the plot range in Fig. 5(c). The purple region represents the 1σ bound of a_e . We can see that there is still parameter space, which can account for the a_e , but have not constrained by the existing experiments (if we don't consider the astrophysical and cosmological constraints).

Based on the method explained in Sec. IV B for the DELPHI experiment, the expected exclusion regions at 95%CL are shown in cyan. We can see that for the operator \mathcal{O}_1 the constraint in low mass region is slightly weaker than the BaBar limit. The reasons are, 1) the cross section for the operator \mathcal{O}_1 decreases with respect to CoM energy; 2) total luminosity of the DELPHI is about a factor of 3 larger than the BaBar's one. On the contrary, for the operator \mathcal{O}_2 , DELPHE's constraint is stronger, because on the one hand cross section of the signal does not depend on s , and on the other hand more background events are killed by the much central cut on $\cos\theta_\gamma$ (see Eq. (22)). We can see that, in small region of m_X , constraint on the Pauli operator already reaches to about 60 TeV, and it is about 2 TeV for the DMTGC operators.

TABLE I. Polarization configures and the corresponding luminosities studied in this paper.

(P_{e-}, P_{e+})	(0, 0)	(+80%, 0)	(+80%, -30%)
$\mathcal{L}_{\text{Int.}} [\text{ab}^{-1}]$	4	1.6	1.6

The black-solid lines show the expected 95%CL experimental sensitivities at the CEPC with an integrated luminosity 5.6 ab^{-1} . The CoM energy of the CEPC is not much higher than the DELPHE's one, but the luminosity is about 40 times larger, hence the expected sensitivity enhanced. For low mass senarios, the mixing parameter can be probed at a level of 7×10^{-4} . The operator \mathcal{O}_2 with an energy scale $\Lambda_2 \sim 600 \text{ TeV}$ can be searched for at the CEPC. Compared to the sensitivities at future Muon collider [34], the CEPC can already probing most of the parameter space. For the operators $\mathcal{O}_{3(4)}$, the 95% sensitivity to $\Lambda_{3(4)}$ can reach to 1 TeV in the whole mass region (within the plot range), and it is about 5 TeV in the low mass region.

B. Significances at ILC

The ILC collider was originally proposed to be run at a CoM energy $\sqrt{s} = 500 \text{ GeV}$ [71], and recently scenarios with $\sqrt{s} = 250 \text{ GeV}$ and $\sqrt{s} = 1 \text{ TeV}$ [72] were also considered. Here we focus the the mode with $\sqrt{s} = 500 \text{ GeV}$, at which data will be collected with a total luminosity of 4 ab^{-1} . In addition, the H20 running scenario [73], in which both electron and positron beams are polarized, was aiming to optimize the physics performance of the experiment. In this paper we consider three polarization configurations, which are listed in the Tab. I. The experimental significances are estimated by applying following kinematical cuts [67],

$$p_{T,\gamma} > 6 \text{ GeV}, \quad |\eta_\gamma| < 2.79. \quad (30)$$

Fig. 6(a), Fig. 6(b) and Fig. 6(c) show the 95%CL sensitivities for the operators \mathcal{O}_1 , \mathcal{O}_2 and $\mathcal{O}_{3(4)}$, respectively. The shades regions are the same as the ones shown in Fig. 5(a)-5(c). For the the operator \mathcal{O}_1 we can see that, even through the total luminosity of the ILC is smaller, and the cross section of the signal is reduced, the experimental sensitivity is enhanced by roughly a factor of 2 for $(P_{e-}, P_{e+}) = (0\%, 0\%)$. This is due to 1) in low energy

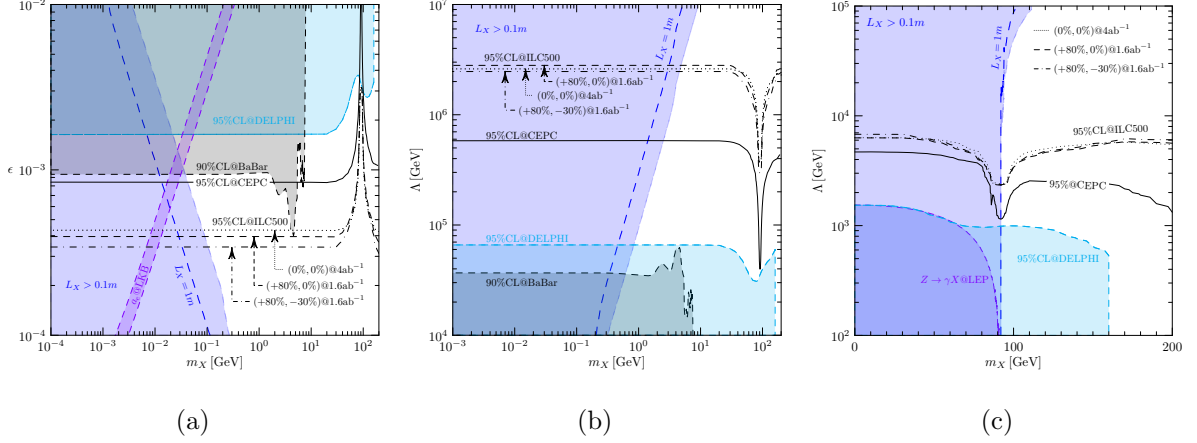


FIG. 6. Expected sensitivities at 95%CL for the operators \mathcal{O}_1 (Fig. 6(a)), \mathcal{O}_2 (Fig. 6(b)) and $\mathcal{O}_{3(4)}$ (Fig. 6(c)) at the ILC500. The shaded regions are the same as the ones shown in Fig. 5. The black-dotted, -dashed, -dashdotted lines show cases for $(P_{e^-}, P_{e^+}) = (0\%, 0\%), (+80\%, 0\%),$ and $(+80\%, -30\%),$ respectively. The 95%CL line for the CEPC is also shown in black-solid line for reference.

region the background also decreases with respect to s as shown in Fig. 3(a); 2) the stronger transverse momentum cut kills more background. However, since the background tends to be a constant at higher s , such enhancement is not expected at colliders with higher CoM energy. On the other hand, as expected the polarization configuration $(P_{e^-}, P_{e^+}) = (+80\%, -30\%)$ gives better sensitivity. But the enhancement is not so promising, since the projected total luminosity is 1.6 ab^{-1} which is smaller than the one of unpolarized scenario by a factor of more than 2. Because of the same reason, polarized beams can not provide sizable optimization for the operators \mathcal{O}_2 and $\mathcal{O}_{3(4)}$, as shown in Fig. 6(b) and Fig. 6(c), respectively. On the other hand, sensitivity to the operator \mathcal{O}_2 is significantly enhanced at the ILC500, and reaches to a level of $\sim 10^3 \text{ TeV}$ which is much higher than the expectation at the future Muon collider [34]. This is due to the distinctive polar angle distribution between the signal and background, as shown in Fig. 2(a), and hence the background is strongly suppressed by the stronger cut $p_{T,\gamma} > 6 \text{ GeV}$. Similar enhancement happens for the operator $\mathcal{O}_{3(4)}$, but it is reduced because the cross section depends on $\Lambda_{3(4)}^{-4}$. On the other hand, probing power in the high mass region is significantly enhanced. The sensitivity at 95%CL can reach to a level of 7 TeV , which is about 5 times larger than the exclusion limit given by $Z \rightarrow \gamma X$ at the LEP and $e^+e^- \rightarrow \gamma X$ by the DELPHE in the low mass region.

VI. CONCLUSION

In summary we studied mono- γ production induced by photon-like, Pauli and DMTGC operators at future e^+e^- colliders. We show that, while energy of the photon is purely determined by kinematics, but polar angle distribution of the photon are very distinctive for the various operators and the background. Particularly, for the DMTGCs, X and γ are generated via a s -channel virtual Z -boson, hence photons are dominantly produced in the central region, as shown in Fig. 2(a). Furthermore, behaviors of the total cross sections at high energy region are also different. While contribution of the photon-like operator decreases as $1/s$, and the one of the Pauli operator does not depend on s , cross sections for the DMTGCs grow quickly with respect to s . Hence at high energy colliders the DMTGC operators are more promising comparing to the Pauli operators.

There were already e^+e^- experiments that searched for dark particles via the mono- γ channel. Focus on the BarBar [51] and DELPHI [52] experiments, we re-interpret the results as constraints on the parameters considered in this work. In small mass region of m_X , constraint from the DELPHI experiment on the Pauli operator already reaches to about 60 TeV, and it is about 2 TeV for the DMTGC operators. We also considered the anomalous magnetic dipole moment of the electron [53, 54]. We show that there is still parameter space, which can account for the a_e , but have not constrained by the existing experiments (except for astrophysical and cosmological constraints). We further studied the expected experimental significance at the CEPC and the ILC. Our results indicate that very high energy colliders, for instance Muon colliders at 3, 10 TeV, can not give much more profound limit on the Pauli operators. This is because cross section for the Pauli operator does not depend on s . The 95% lower limit on Λ_2 can reach to 600 TeV at the CEPC, and can be enhanced to $\sim 10^3$ TeV at ILC500. On the other hand, because production rates induced by the DMTGC operators grow quickly as increasing s , it is more interesting to search for signals of the DMTGC at high energy colliders. The expected lower limit of $\Lambda_{3(4)}$ at 95%CL is about 5 TeV at the CEPC, and it is about 7 TeV at the ILC500. Possible enhancement by beam polarization are also studied. However, because of its smaller integrated luminosity, the bounds on the scale parameters can only be enhanced slightly.

ACKNOWLEDGMENTS

K.M. was supported by the Innovation Capability Support Program of Shaanxi Province (Program No. 2021KJXX-47).

- [1] G. Bertone, D. Hooper and J. Silk, *Particle dark matter: Evidence, candidates and constraints*, *Phys. Rept.* **405** (2005) 279 [[hep-ph/0404175](#)].
- [2] PLANCK collaboration, *Planck 2018 results. VI. Cosmological parameters*, *Astron. Astrophys.* **641** (2020) A6 [[1807.06209](#)].
- [3] A.M. Green, *Dark matter in astrophysics/cosmology*, *SciPost Phys. Lect. Notes* **37** (2022) 1 [[2109.05854](#)].
- [4] R. Capdevilla, D. Curtin, Y. Kahn and G. Krnjaic, *Systematically Testing Singlet Models for $(g - 2)_\mu$* , [2112.08377](#).
- [5] A. Birkedal, K. Matchev and M. Perelstein, *Dark matter at colliders: A Model independent approach*, *Phys. Rev. D* **70** (2004) 077701 [[hep-ph/0403004](#)].
- [6] Y.J. Chae and M. Perelstein, *Dark Matter Search at a Linear Collider: Effective Operator Approach*, *JHEP* **05** (2013) 138 [[1211.4008](#)].
- [7] B. Barman, S. Bhattacharya, S. Girmohanta and S. Jahedi, *Catch 'em all: Effective Leptophilic WIMPs at the $e^+ e^-$ Collider*, [2109.10936](#).
- [8] A. Crivellin, F. D'Eramo and M. Procura, *New Constraints on Dark Matter Effective Theories from Standard Model Loops*, *Phys. Rev. Lett.* **112** (2014) 191304 [[1402.1173](#)].
- [9] R.J. Hill and M.P. Solon, *Standard Model anatomy of WIMP dark matter direct detection I: weak-scale matching*, *Phys. Rev. D* **91** (2015) 043504 [[1401.3339](#)].
- [10] G. Bertone and T. Tait, M. P., *A new era in the search for dark matter*, *Nature* **562** (2018) 51 [[1810.01668](#)].
- [11] J. Billard et al., *Direct Detection of Dark Matter – APPEC Committee Report*, [2104.07634](#).
- [12] J.M. Gaskins, *A review of indirect searches for particle dark matter*, *Contemp. Phys.* **57** (2016) 496 [[1604.00014](#)].
- [13] A. Boveia and C. Doglioni, *Dark Matter Searches at Colliders*, *Ann. Rev. Nucl. Part. Sci.* **68** (2018) 429 [[1810.12238](#)].

- [14] E. Del Nobile and F. Sannino, *Dark Matter Effective Theory*, *Int. J. Mod. Phys. A* **27** (2012) 1250065 [[1102.3116](#)].
- [15] M. Duch, B. Grzadkowski and J. Wudka, *Classification of effective operators for interactions between the Standard Model and dark matter*, *JHEP* **05** (2015) 116 [[1412.0520](#)].
- [16] J. Brod, A. Gootjes-Dreesbach, M. Tammara and J. Zupan, *Effective Field Theory for Dark Matter Direct Detection up to Dimension Seven*, *JHEP* **10** (2018) 065 [[1710.10218](#)].
- [17] J.C. Criado, A. Djouadi, M. Perez-Victoria and J. Santiago, *A complete effective field theory for dark matter*, *JHEP* **07** (2021) 081 [[2104.14443](#)].
- [18] J. Aebischer, W. Altmannshofer, E.E. Jenkins and A.V. Manohar, *Dark Matter Effective Field Theory and an Application to Vector Dark Matter*, [2202.06968](#).
- [19] A. De Simone, A. Monin, A. Thamm and A. Urbano, *On the effective operators for Dark Matter annihilations*, *JCAP* **02** (2013) 039 [[1301.1486](#)].
- [20] S. Matsumoto, S. Mukhopadhyay and Y.-L.S. Tsai, *Effective Theory of WIMP Dark Matter supplemented by Simplified Models: Singlet-like Majorana fermion case*, *Phys. Rev. D* **94** (2016) 065034 [[1604.02230](#)].
- [21] S. Matsumoto, S. Mukhopadhyay and Y.-L.S. Tsai, *Singlet Majorana fermion dark matter: a comprehensive analysis in effective field theory*, *JHEP* **10** (2014) 155 [[1407.1859](#)].
- [22] H. Han, H. Wu and S. Zheng, *Effective field theory of the Majorana dark matter*, *Chin. Phys. C* **43** (2019) 043103 [[1711.10097](#)].
- [23] M. Pospelov, *Secluded $U(1)$ below the weak scale*, *Phys. Rev. D* **80** (2009) 095002 [[0811.1030](#)].
- [24] B. Holdom, *Two $U(1)$'s and Epsilon Charge Shifts*, *Phys. Lett. B* **166** (1986) 196.
- [25] M. Fabbrichesi, E. Gabrielli and G. Lanfranchi, *The Dark Photon*, [2005.01515](#).
- [26] R. Essig et al., *Working Group Report: New Light Weakly Coupled Particles*, in *Community Summer Study 2013: Snowmass on the Mississippi*, 10, 2013 [[1311.0029](#)].
- [27] J. Alexander et al., *Dark Sectors 2016 Workshop: Community Report*, 8, 2016 [[1608.08632](#)].
- [28] M.A. Deliyergiyev, *Recent Progress in Search for Dark Sector Signatures*, *Open Phys.* **14** (2016) 281 [[1510.06927](#)].
- [29] P. Ilten, Y. Soreq, M. Williams and W. Xue, *Serendipity in dark photon searches*, *JHEP* **06** (2018) 004 [[1801.04847](#)].

- [30] M. Bauer, P. Foldenauer and J. Jaeckel, *Hunting All the Hidden Photons*, *JHEP* **07** (2018) 094 [[1803.05466](#)].
- [31] S.-F. Ge, X.-D. Ma and P. Pasquini, *Probing the dark axion portal with muon anomalous magnetic moment*, *Eur. Phys. J. C* **81** (2021) 787 [[2104.03276](#)].
- [32] B.A. Dobrescu, *Massless gauge bosons other than the photon*, *Phys. Rev. Lett.* **94** (2005) 151802 [[hep-ph/0411004](#)].
- [33] E. Gabrielli, B. Mele, M. Raidal and E. Venturini, *FCNC decays of standard model fermions into a dark photon*, *Phys. Rev. D* **94** (2016) 115013 [[1607.05928](#)].
- [34] M. Casarsa, M. Fabbrichesi and E. Gabrielli, *Monochromatic single photon events at the muon collider*, *Phys. Rev. D* **105** (2022) 075008 [[2111.13220](#)].
- [35] H. Georgi, *On-shell effective field theory*, *Nucl. Phys. B* **361** (1991) 339.
- [36] K.J.F. Gaemers and G.J. Gounaris, *Polarization Amplitudes for $e^+ e^- \rightarrow W^+ W^-$ and $e^+ e^- \rightarrow Z Z$* , *Z. Phys. C* **1** (1979) 259.
- [37] K. Hagiwara, R.D. Peccei, D. Zeppenfeld and K. Hikasa, *Probing the Weak Boson Sector in $e^+ e^- \rightarrow W^+ W^-$* , *Nucl. Phys. B* **282** (1987) 253.
- [38] F.M. Renard, *Tests of Neutral Gauge Boson Selfcouplings With $e^+ e^- \rightarrow \gamma Z$* , *Nucl. Phys. B* **196** (1982) 93.
- [39] A. Barroso, F. Boudjema, J. Cole and N. Dombey, *Electromagnetic Properties of the Z Boson. 1.*, *Z. Phys. C* **28** (1985) 149.
- [40] G.J. Gounaris, J. Layssac and F.M. Renard, *Signatures of the anomalous Z_γ and ZZ production at the lepton and hadron colliders*, *Phys. Rev. D* **61** (2000) 073013 [[hep-ph/9910395](#)].
- [41] G.-W. Yuan, L. Zu, L. Feng and Y.-F. Cai, *W-boson mass anomaly: probing the models of axion-like particle, dark photon and Chameleon dark energy*, [2204.04183](#).
- [42] J.A. Dror, R. Lasenby and M. Pospelov, *New constraints on light vectors coupled to anomalous currents*, *Phys. Rev. Lett.* **119** (2017) 141803 [[1705.06726](#)].
- [43] B. Batell, D. McKeen and M. Pospelov, *New Parity-Violating Muonic Forces and the Proton Charge Radius*, *Phys. Rev. Lett.* **107** (2011) 011803 [[1103.0721](#)].
- [44] L3 collaboration, *Search for new physics in energetic single photon production in $e^+ e^-$ annihilation at the Z resonance*, *Phys. Lett. B* **412** (1997) 201.

- [45] DELPHI collaboration, *Search for neutral heavy leptons produced in Z decays*, *Z. Phys. C* **74** (1997) 57.
- [46] A. Alloul, N.D. Christensen, C. Degrande, C. Duhr and B. Fuks, *FeynRules 2.0 - A complete toolbox for tree-level phenomenology*, *Comput. Phys. Commun.* **185** (2014) 2250 [[1310.1921](#)].
- [47] J. Alwall, R. Frederix, S. Frixione, V. Hirschi, F. Maltoni, O. Mattelaer et al., *The automated computation of tree-level and next-to-leading order differential cross sections, and their matching to parton shower simulations*, *JHEP* **07** (2014) 079 [[1405.0301](#)].
- [48] K. Yokoya, *Quantum Correction to Beamstrahlung Due to the Finite Number of Photons*, *Nucl. Instrum. Meth. A* **251** (1986) 1.
- [49] C. Chen, Z. Cui, G. Li, Q. Li, M. Ruan, L. Wang et al., *$H \rightarrow e^+e^-$ at CEPC: ISR effect with MadGraph*, [1705.04486](#).
- [50] Q. Li and Q.-S. Yan, *Initial State Radiation Simulation with MadGraph*, [1804.00125](#).
- [51] BABAR collaboration, *Search for Invisible Decays of a Dark Photon Produced in e^+e^- Collisions at BaBar*, *Phys. Rev. Lett.* **119** (2017) 131804 [[1702.03327](#)].
- [52] DELPHI collaboration, *Search for one large extra dimension with the DELPHI detector at LEP*, *Eur. Phys. J. C* **60** (2009) 17 [[0901.4486](#)].
- [53] L. Morel, Z. Yao, P. Cladé and S. Guellati-Khélifa, *Determination of the fine-structure constant with an accuracy of 81 parts per trillion*, *Nature* **588** (2020) 61.
- [54] L. Darmé, F. Giacchino, E. Nardi and M. Raggi, *Invisible decays of axion-like particles: constraints and prospects*, *JHEP* **06** (2021) 009 [[2012.07894](#)].
- [55] BABAR collaboration, *Search for a Dark Photon in e^+e^- Collisions at BaBar*, *Phys. Rev. Lett.* **113** (2014) 201801 [[1406.2980](#)].
- [56] P.J. Fox, R. Harnik, J. Kopp and Y. Tsai, *LEP Shines Light on Dark Matter*, *Phys. Rev. D* **84** (2011) 014028 [[1103.0240](#)].
- [57] DELPHI collaboration, *Photon events with missing energy in e^+e^- collisions at $s^{**}(1/2) = 130\text{-GeV}$ to 209-GeV* , *Eur. Phys. J. C* **38** (2005) 395 [[hep-ex/0406019](#)].
- [58] T. Aoyama et al., *The anomalous magnetic moment of the muon in the Standard Model*, *Phys. Rept.* **887** (2020) 1 [[2006.04822](#)].
- [59] A. Keshavarzi, K.S. Khaw and T. Yoshioka, *Muon $g - 2$: A review*, *Nucl. Phys. B* **975** (2022) 115675 [[2106.06723](#)].

- [60] MUON G-2 collaboration, *Measurement of the Positive Muon Anomalous Magnetic Moment to 0.46 ppm*, *Phys. Rev. Lett.* **126** (2021) 141801 [[2104.03281](#)].
- [61] MUON G-2 collaboration, *Final Report of the Muon E821 Anomalous Magnetic Moment Measurement at BNL*, *Phys. Rev. D* **73** (2006) 072003 [[hep-ex/0602035](#)].
- [62] R.H. Parker, C. Yu, W. Zhong, B. Estey and H. Müller, *Measurement of the fine-structure constant as a test of the Standard Model*, *Science* **360** (2018) 191 [[1812.04130](#)].
- [63] T. Aoyama, T. Kinoshita and M. Nio, *Revised and Improved Value of the QED Tenth-Order Electron Anomalous Magnetic Moment*, *Phys. Rev. D* **97** (2018) 036001 [[1712.06060](#)].
- [64] P. Fayet, *U-boson production in e^+e^- annihilations, ψ and Upsilon decays, and Light Dark Matter*, *Phys. Rev. D* **75** (2007) 115017 [[hep-ph/0702176](#)].
- [65] NA64 collaboration, *Search for Axionlike and Scalar Particles with the NA64 Experiment*, *Phys. Rev. Lett.* **125** (2020) 081801 [[2005.02710](#)].
- [66] K. Mimasu and V. Sanz, *ALPs at Colliders*, *JHEP* **06** (2015) 173 [[1409.4792](#)].
- [67] M. Habermehl, M. Berggren and J. List, *WIMP Dark Matter at the International Linear Collider*, *Phys. Rev. D* **101** (2020) 075053 [[2001.03011](#)].
- [68] S. Kundu, A. Guha, P.K. Das and P.S.B. Dev, *A model-independent analysis of leptophilic dark matter at future electron-positron colliders in the mono-photon and mono-Z channels*, [2110.06903](#).
- [69] CEPC STUDY GROUP collaboration, *CEPC Conceptual Design Report: Volume 2 - Physics \mathcal{E} Detector*, [1811.10545](#).
- [70] Z. Liu, Y.-H. Xu and Y. Zhang, *Probing dark matter particles at CEPC*, *JHEP* **06** (2019) 009 [[1903.12114](#)].
- [71] P. Bambade et al., *The International Linear Collider: A Global Project*, [1903.01629](#).
- [72] K. Fujii et al., *Physics Case for the 250 GeV Stage of the International Linear Collider*, [1710.07621](#).
- [73] T. Barklow, J. Brau, K. Fujii, J. Gao, J. List, N. Walker et al., *ILC Operating Scenarios*, [1506.07830](#).